

Quantum-inspired Bayesian probability algorithm for nuclear mass predictions

Kaizhong Tan*, Jian Liu*[†], and Chuan Wang

College of Science, China University of Petroleum (East China), Qingdao 266580, China

In this study, a novel quantum-inspired Bayesian probability (QIBP) algorithm, informed by quantum dynamics, is proposed to improve the predictions of nuclear mass from theoretical models. Within the QIBP framework, residuals between the theoretical and experimental mass values are mapped into wave functions in Hilbert space. The corresponding potentials are obtained by solving the Schrödinger equation. Assuming that the residuals follow a Boltzmann distribution, the prior and likelihood probability density functions (PDFs) can be obtained from potentials. Finally, the Bayesian theorem is applied to derive the posterior PDF for estimating the target nuclear mass residuals. Global optimization and extrapolation analyses indicate that the QIBP algorithm effectively captures quantum effects and subtle patterns, which are not fully incorporated into theoretical models, thereby providing reliable predictions. In addition, the extrapolation based on the “synthetic experimental set” further evaluates the performance and applicability of the QIBP algorithm across the entire nuclear chart. Furthermore, the QIBP algorithm is applied to predict α -decay energies of Ra and Es isotopes, and the shell effects manifested in these isotopes are analyzed. This study validates the feasibility of quantum machine learning in nuclear mass research, and demonstrates that the proposed algorithm can accurately describe nuclear masses, with potential applications in other areas of nuclear physics.

I. INTRODUCTION

Machine learning (ML) has recently advanced at an unprecedented rate, achieving breakthroughs in various areas of fundamental science [1–4]. In 2024, the Nobel Prize in Physics was awarded for the development of ML algorithms based on physical principles [5–9], and the Nobel Prize in Chemistry honored the use of ML in the prediction of protein structure [10–13]. Recognizing the quantum nature of the world has prompted researchers to embed well-established classical theories into quantum Hilbert space. For example, Shannon’s information theory has evolved into quantum information theory [14], and Turing’s theory of computation has given rise to quantum computing [15]. Like other classical theories, ML can also be reformulated within a quantum-mechanical framework. Embedding superposition [16], entanglement [17], and quantum-dynamic features [18] into ML algorithms can overcome the computational bottlenecks of classical methods, enhance data mining capabilities, and discover novel solutions to specific problems. As a result, the field of quantum machine learning (QML) has emerged [19]. It is widely regarded as a promising future direction for ML and is expected to provide powerful tools to accelerate scientific discovery [20]. Particularly, QML is more likely to exhibit quantum advantage when handling data originating from quantum-mechanical processes, such as from experiments in physical chemistry [21, 22] and high-energy physics [23–27]. Given that atomic nuclei are complex quantum many-body systems, combining QML with nuclear physics holds great potential.

There are mainly two categories of QML algorithms. [28]. The first class is designed to utilize quantum parallelism to accelerate the training of the ML model. It preserves the classical ML framework while implementing complex computations on quantum hardware. Representative examples include quantum principal component analysis [29–32] and quantum support vector machines [33–35]. The second class explores similarities between quantum systems and ML processes to develop new algorithms. The entire process of algorithms within this class can be implemented on classical computers, yet they offer more distinctive and advantageous solutions than existing ML algorithms. Such research is still limited, with notable works including the quantum clustering (QC) algorithm [36, 37] and the tensor networks [38, 39]. Overall, different types of QML possess distinct advantages and can be flexibly applied based on specific problems.

The nuclear mass is the most fundamental property of nuclei, as it reflects the interactions among all constituents of the nucleus [40]. It is crucial for nuclear and astrophysical studies to explore the limits of nuclear existence [41, 42], reveal shell evolution [43, 44], and understand the abundance of elements [45, 46]. Theoretical models for determining nuclear masses rely on different physical assumptions [47–52], such as spherical symmetry [53, 54] and local correlation [55–57]. In unknown regions far from the β -stability, the predictions of different models can differ by several to tens of MeV [58]. Hence, there is considerable scope for improving the existing nuclear mass models. In recent years, ML has emerged as a powerful tool for improving the nuclear mass predictions [59, 60], with approaches including neural networks [61–69], tree-based algorithms [70, 71], Bayesian inference [72–78], and regression models [79, 80] achieving notable success. These data-driven methods identify complex relationships between nuclear mass data and relevant features, and capture subtle patterns and correlations that

* The two authors contributed equally to this work.

[†] Contact author: liujian@upc.edu.cn

might be overlooked by theoretical models, thus exhibiting superior generalization capabilities. Many studies have reduced the standard deviation in nuclear mass predictions to below 200 keV, and several newly proposed magic numbers have been validated [81]. These advancements offer crucial support for studies of exotic nuclear structures and the r -process [82].

Both the theoretical description and the experimental determination of nuclear masses are closely related to quantum mechanics [83, 84]. Compared with classical ML, QML can describe quantum systems more naturally and is therefore suited to nuclear mass predictions. This study proposes a quantum-inspired Bayesian probability (QIBP) algorithm to improve nuclear mass predictions. In the QIBP framework, the residuals δ between theoretical and experimental mass values are treated as states in Hilbert space and mapped to wave functions ψ . By treating ψ as eigenstates of the Schrödinger equation, the potentials are derived through simple analytical operations. Assuming that the residuals follow a Boltzmann distribution, the prior and likelihood probability density functions (PDFs) can be obtained from the Schrödinger potentials. Finally, the posterior PDF is determined via Bayesian theory, and its expectation value is evaluated to provide a precise estimate of the residual δ , which is then used to optimize the theoretical models.

In this study, the QIBP algorithm is applied to two representative theoretical models, the macroscopic-microscopic WS4 model [85] and the microscopic Hartree-Fock-Bogoliubov (HFB) model with the SLy4 parameter set [86]. Global optimization and extrapolation analyses are performed to evaluate the capability of the QIBP algorithm to optimize theoretical models and to capture quantum effects and other subtle patterns. In addition, the advantages of the QML algorithm are discussed through a comparison with classical Bayesian inference methods. Finally, α -decay energies of Ra and Es isotopes are predicted using the QIBP algorithm, and subshell effects exhibited by the Es isotopes are analyzed. Results show that the QIBP algorithm can provide accurate predictions for nuclear masses of unknown nuclei, with potential applications in other areas of nuclear physics, such as nuclear reactions and astrophysics.

The structure of this paper is as follows: Sec. II discusses the theoretical framework of the QIBP algorithm; Sec. III presents the results and related analyses of the QIBP algorithm; and Sec. IV provides the conclusion.

II. THEORETICAL FRAMEWORK

This section introduces the theoretical framework of the quantum-inspired Bayesian probability (QIBP) algorithm. The QIBP algorithm is designed to predict the residuals between theoretical and experimental nuclear mass values, thereby improving the performance of theoretical models. Its structure consists of two principal components: an external framework constructed using

Bayesian theory, and a core module designed for probability density estimation based on quantum dynamical principles.

A. The multivariate Bayesian theorem

The external framework of the QIBP algorithm is based on the multivariate Bayesian theorem, which forms its classical part. In the QIBP algorithm, the residual δ of nuclear mass is treated as a continuous variable. For a target nucleus with proton number Z_t and neutron number N_t , it is assumed that Z_t and N_t are independent features. According to the multivariate Bayesian theorem, the posterior probability density function (PDF) of δ for the target nucleus (Z_t, N_t) can be expressed as

$$p(\delta|Z_t, N_t) = \frac{p(Z_t|\delta)p(N_t|\delta)p(\delta)}{\int p(Z_t|\delta)p(N_t|\delta)p(\delta)d\delta}. \quad (1)$$

The likelihood PDFs $p(Z_t|\delta)$ and $p(N_t|\delta)$ in Eq. (1) can be obtained by the univariate Bayesian formula,

$$p(Z_t|\delta) = \frac{p(\delta|Z_t)p(Z_t)}{p(\delta)}, \quad (2)$$

$$p(N_t|\delta) = \frac{p(\delta|N_t)p(N_t)}{p(\delta)}. \quad (3)$$

The prior probabilities $p(Z_t)$ and $p(N_t)$ depend on the frequencies of occurrence of nuclei with the same proton number Z_t and the neutron number N_t in the dataset, respectively. Note that if the dataset lacks nuclides with the same proton or neutron number as the target nucleus, the likelihood PDF $p(Z_t|\delta)$ or $p(N_t|\delta)$ is treated as a constant in Eq. (1). Since the posterior PDF is normalized afterward, the choice of this constant does not affect the final result. To calculate the posterior PDF of δ , it is sufficient to determine three PDFs, the prior PDF $p(\delta)$, and two likelihood PDFs, $p(\delta|Z_t)$ and $p(\delta|N_t)$.

B. Quantum-inspired determination of probability density functions

The core of the QIBP algorithm is applying concepts from quantum dynamics, including wave functions and the Schrödinger equation, to determine the three probability density functions described in Sec. II A. The residuals are first mapped to wave functions in Hilbert space, from which the corresponding potentials are obtained by solving the Schrödinger equation. Assuming that the residuals follow a Boltzmann distribution, the PDFs can be derived from the potentials. Specifically, for a dataset containing n residual data points, under the assumption that they follow a Gaussian distribution, the wave function $\Psi(\delta)$ of the target nucleus (Z_t, N_t) is defined as

$$\Psi(\delta) = \sum_{i=1}^n e^{-\frac{(\delta-\delta_i)^2}{2\lambda^2}}, \quad (4)$$

where $\delta_i = \delta_i^{\text{exp}} - \delta_i^{\text{th}}$ represents the raw residual of each nucleus in the dataset. To effectively predict nuclear masses, a weight coefficient $w_{i,t}$ is introduced to capture local features,

$$w_{i,t} = \exp\left[-\frac{(Z_i - Z_t)^2 + (N_i - N_t)^2}{2}\right]. \quad (5)$$

After introducing the weight coefficients, the wave function is expressed as

$$\psi_t(\delta) = \sum_{i=1}^n w_{i,t} e^{-\frac{(\delta-\delta_i)^2}{2\lambda^2}}. \quad (6)$$

To determine the likelihood PDFs $p(\delta|Z_t)$ and $p(\delta|N_t)$, wave functions associated with the isotopic and isotonic chains are also derived using the same procedure,

$$\psi_{Z_t}(\delta) = \sum_{i=1}^{n_Z} w_{i,t} e^{-\frac{(\delta-\delta_i)^2}{2\lambda^2}}, \quad (7)$$

$$\psi_{N_t}(\delta) = \sum_{i=1}^{n_N} w_{i,t} e^{-\frac{(\delta-\delta_i)^2}{2\lambda^2}}. \quad (8)$$

Here, $n_Z(n_N)$ represents the number of nuclei with $Z_t(N_t)$. When constructing $\psi_{Z_t}(\delta)$ and $\psi_{N_t}(\delta)$, only the nuclei in the dataset that have the same proton number Z_t or the same neutron number N_t as the target nucleus are considered. The QIBP algorithm treats $\psi_t(\delta)$, $\psi_{Z_t}(\delta)$, and $\psi_{N_t}(\delta)$ as eigenstates of the Schrödinger equation,

$$H\psi = \left[-\frac{\lambda^2}{2} \frac{d^2}{d\delta^2} + V\right] \psi = E\psi. \quad (9)$$

Here we rescaled H and V of the conventional quantum-mechanical equation to leave only one parameter λ . The potentials $V_t(\delta)$, $V_{Z_t}(\delta)$, and $V_{N_t}(\delta)$ are derived by solving Eq. (9),

$$V_t(\delta) = E_t - \frac{1}{2} + \frac{1}{2\lambda^2\psi_t(\delta)} \sum_{i=1}^n w_{i,t} (\delta-\delta_i)^2 e^{-\frac{(\delta-\delta_i)^2}{2\lambda^2}}, \quad (10)$$

$$V_{Z_t}(\delta) = E_{Z_t} - \frac{1}{2} + \frac{1}{2\lambda^2\psi_{Z_t}(\delta)} \sum_{i=1}^{n_Z} w_{i,t} (\delta-\delta_i)^2 e^{-\frac{(\delta-\delta_i)^2}{2\lambda^2}}, \quad (11)$$

$$V_{N_t}(\delta) = E_{N_t} - \frac{1}{2} + \frac{1}{2\lambda^2\psi_{N_t}(\delta)} \sum_{i=1}^{n_N} w_{i,t} (\delta-\delta_i)^2 e^{-\frac{(\delta-\delta_i)^2}{2\lambda^2}}. \quad (12)$$

By further requiring that the minimum value of V is zero, we obtain

$$E = -\min \frac{\lambda^2}{2\psi} \frac{d^2\psi}{d\delta^2}, \quad (13)$$

thereby uniquely determining E_t , E_{Z_t} , E_{N_t} in Eqs. (10)-(12).

As a prominent QML method, the quantum clustering (QC) algorithm was the first to employ such potentials for data classification and conducted an in-depth analysis of their robustness. Since the potential contains information from both the second derivative and the gradient of the wave function ψ , it offers greater sensitivity and robustness in data processing. From a physical perspective, the minima of V act as abstract gravitational sources, attracting the distribution of δ toward more stable (lower-energy) regions. The potential thus represents this trend as a correction and captures the quantum dynamical features of the δ distribution.

The purpose of this work is not to perform clustering through the potential. Instead, the potential is used to extract the probability density distribution of δ . The well-known Boltzmann machine employs the mathematical form of the Boltzmann distribution to derive probability density functions from an energy function [87, 88]. This study adopts a similar approach. Assuming that the residuals follow a Boltzmann distribution, the prior PDF $p(\delta)$ and the likelihood PDFs $p(\delta|Z_t)$ and $p(\delta|N_t)$ can be derived from the corresponding potentials,

$$p(\delta) = \frac{1}{C_t} e^{-\beta V_t(\delta)}, \quad (14)$$

$$p(\delta|Z_t) = \frac{1}{C_{Z_t}} e^{-\beta_Z V_{Z_t}(\delta)}, \quad (15)$$

$$p(\delta|N_t) = \frac{1}{C_{N_t}} e^{-\beta_N V_{N_t}(\delta)}, \quad (16)$$

where C_t , C_{Z_t} , and C_{N_t} normalize the three PDFs, and the smoothing parameters β , β_Z , and β_N affect the stability of the PDFs, respectively. By substituting the three PDFs into Eqs. (1)-(3) of the Bayesian framework, the posterior PDF $p(\delta|Z_t, N_t)$ for the target nucleus (Z_t, N_t) is obtained. The final estimated residual for the target nucleus is then determined by calculating the expectation value,

$$\delta^{\text{em}}(Z_t, N_t) = \int \delta p(\delta|Z_t, N_t) d\delta. \quad (17)$$

Finally, the refined mass prediction $E^{\text{corr}}(Z_t, N_t)$ is obtained by adding the estimated residual to the theoretical mass $E^{\text{th}}(Z_t, N_t)$,

$$E^{\text{corr}}(Z_t, N_t) = E^{\text{th}}(Z_t, N_t) + \delta^{\text{em}}(Z_t, N_t). \quad (18)$$

The standard deviation σ_{rms} is used to quantify the deviation between the refined predictions and the exper-

imental data. It is defined as

$$\sigma_{\text{rms}}^2 = \frac{1}{n} \sum_{i=1}^n (E_i^{\text{corr}} - E_i^{\text{exp}})^2. \quad (19)$$

In the QIBP algorithm, the predicted uncertainty is derived from the posterior PDF. The one-sigma uncertainty associated with the prediction for the nucleus (Z_t, N_t) is given by

$$\Delta E(Z_t, N_t) = \sqrt{\int [\delta - \delta^{\text{em}}(Z_t, N_t)]^2 p(\delta|Z_t, N_t) d\delta}. \quad (20)$$

III. RESULTS AND DISCUSSION

This section presents the performance of the QIBP algorithm in improving nuclear mass predictions. AME2020 compiles the nuclear masses of 3557 nuclides, of which 2457 are determined experimentally and 1100 are estimated. To ensure the rigor of this study, only nuclides with experimentally measured masses are considered. A total of 2253 nuclei with proton number $Z \geq 20$ and neutron number $N \geq 20$ from AME2020 [89] are selected as the entire set. All nuclear mass data used in this study are experimentally measured values. Theoretical models employed in this study include the macroscopic-microscopic WS4 model [85] and the microscopic Hartree-Fock-Bogoliubov (HFB) model with the SLy4 parameter set [86]. The theoretical mass values of 2253 nuclei are first calculated from these models, and the corresponding residuals are determined as $\delta^{\text{pre}} = E^{\text{exp}} - E^{\text{th}}$. The QIBP algorithm is then applied to optimize the predictions of each model. Global optimization and extrapolation analyzes are performed to assess the effectiveness of the QIBP algorithm in refining theoretical models and capturing subtle patterns. Finally, the predictive capability of the QIBP algorithm for α -decay energies is demonstrated.

In determining the three PDFs $p(\delta)$, $p(\delta|Z_t)$, and $p(\delta|N_t)$, there are three undefined parameters, β , β_Z , and β_N . In general, $p(\delta)$ describes the global distribution of nuclear mass residuals and should be modeled smoothly to mitigate noise. $p(\delta|Z_t)$ and $p(\delta|N_t)$ describe local residual distributions and typically require finer resolution. To ensure the stability of the QIBP algorithm, a basic guideline is that β should be smaller than β_Z and β_N . Under this condition, the QIBP algorithm achieves robust optimization performance. Ultimately, the general parameter combination for the QIBP algorithm is set as $\beta = 1/1.6$, $\beta_Z = 1/0.8$, and $\beta_N = 1/1.2$.

A. Global optimizations of the QIBP algorithm

Leave-one-out cross-validation is employed in global optimization analysis. Specifically, when predicting the

mass of a target nucleus, the remaining 2252 nuclei in the entire set are used as the learning set. Following the procedure described in Sec. II, the wave functions ψ are determined by Eqs. (6)-(8), and the corresponding potential V are obtained from Eqs. (10)-(12). Within the Bayesian framework, the posterior PDF $p(\delta|Z_t, N_t)$ is determined by integrating Eqs. (1)-(3). The refined nuclear mass is finally calculated using Eqs. (17) and (18). The same calculation is applied to each nucleus in the entire set. To demonstrate the optimization performance of the QIBP algorithm, Table I presents the standard deviations before and after optimization, denoted as σ^{pre} and σ^{post} , respectively. The improvement rates achieved by the QIBP algorithm are quantified as $\Delta\sigma/\sigma^{\text{pre}} = (\sigma^{\text{pre}} - \sigma^{\text{post}})/\sigma^{\text{pre}}$. In addition, the distributions of the residuals before and after optimization across the nuclear chart are illustrated in Fig. 1.

TABLE I. Standard deviations σ_{pre} (MeV) from the WS4 and HFB models, as well as σ_{post} (MeV) after QIBP and CBP refinements. A total of 2253 nuclei in AME2020 with $Z \geq 20$ and $N \geq 20$ are chosen as the entire set.

Models	σ_{pre}	QIBP		CBP	
		σ_{post}	$\Delta\sigma/\sigma_{\text{pre}}$	σ_{post}	$\Delta\sigma/\sigma_{\text{pre}}$
WS4	0.273	0.149	45.4%	0.187	31.5%
HFB	5.250	0.324	93.8%	0.509	90.3%

Table I demonstrates that the QIBP algorithm enhances the performance of both theoretical models. For the WS4 model, the standard deviation is reduced from $\sigma_{\text{pre}} = 0.273$ MeV to $\sigma_{\text{post}} = 0.149$ MeV, corresponding to an improvement rate of 45.4%. In addition to the improvement in overall standard deviation, changes in the residual distribution across the nuclear chart can further demonstrate the optimization capability of the QIBP algorithm. As shown in Fig. 1(a), before applying the QIBP algorithm, patterns in the residuals distribution remain observable. Some regions show clusters of positive residuals, indicated by concentrated red areas, while others are dominated by negative residuals, appearing as blue zones. This clustering pattern of residuals indicates that certain physical effects are still not incorporated into the WS4 model. In addition, the residuals exhibit a certain level of odd-even staggering, suggesting that this effect is not fully captured by the WS4 model. After applying the QIBP algorithm, the residuals are reduced across the entire nuclear chart. The distribution of residuals becomes more random, and the odd-even staggering is weakened. This suggests that the QIBP algorithm effectively incorporates patterns and correlations overlooked by the WS4 model, resulting in a lower standard deviation.

For the HFB model, the standard deviation is reduced from $\sigma^{\text{pre}} = 5.250$ MeV to $\sigma^{\text{post}} = 0.324$ MeV, corresponding to an improvement rate of 93.8%. In Fig. 1(c), the residuals of the HFB model before optimization are large and exhibit a clearer pattern. In regions near proton

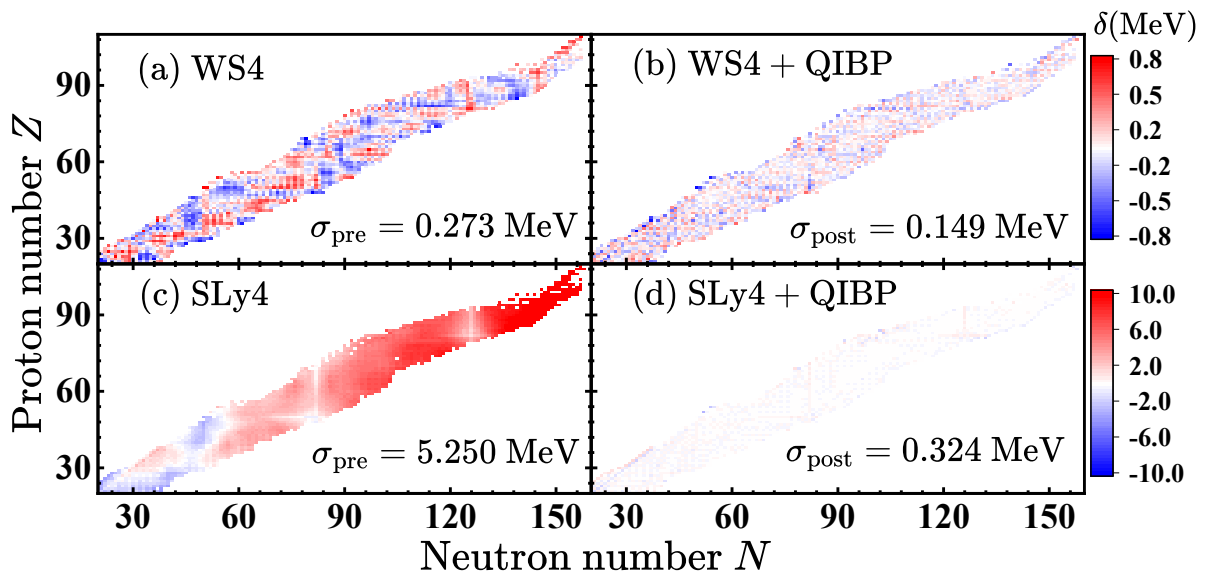


FIG. 1. (a) The raw nuclear mass residuals δ (MeV) from the WS4 model. (b) The nuclear mass residuals from the WS4 model after refinement by the QIBP algorithm. (c) The same as (a), but for the HFB model. (d) The same as (b), but for the HFB model after refinement by the QIBP algorithm.

and neutron magic numbers, the mass deviations are significantly smaller than those in surrounding areas. This is because the HFB model with the SLy4 parameter set is solved under the assumption of spherical symmetry and does not account for deformation effects. As a result, the HFB model provides accurate descriptions of doubly magical nuclei, but shows systematic deviations for deformed nuclei. Fig. 1(d) illustrates that the QIBP algorithm identifies correlations in mass residuals and effectively captures deformation effects not included in the HFB model, thereby enabling improved descriptions of nuclear mass.

The above discussion indicates that, building on the global descriptions provided by theoretical models, the QIBP algorithm can further capture patterns that are not taken into account by these models, thereby achieving effective refinement. The performance of the QIBP algorithm originates from its theoretical framework. As a QML approach, the PDFs are derived from the Schrödinger potential, thereby introducing quantum dynamical corrections. These PDFs exhibit strong robustness and are capable of accurately capturing underlying quantum effects from nuclear mass residual data, such as odd-even staggering and deformation. In addition, the Bayesian framework, together with the weight coefficients, incorporates statistical correlations among neighboring nuclei, all of which contribute to reliable and precise predictions.

To demonstrate the advantage of the QIBP algorithm over the classical Bayesian approach, Table I also presents the prediction results of the continuous Bayesian probability (CBP) estimator for nuclear mass [77, 78]. The CBP estimator obtains the prior PDFs and the likelihood PDFs of the residuals through kernel density es-

timation (KDE). Then, it employs Bayesian theory to determine the posterior PDF and the expected value of the residuals. After optimization with the CBP estimator, the standard deviations of the WS4 and HFB models are reduced to 0.187 MeV and 0.509 MeV, respectively. This indicates that the predictive capability of the CBP estimator for nuclear masses is weaker than that of the QIBP algorithm.

Moreover, we perform an in-depth comparison between the QIBP algorithm and the CBP estimator. Fig. 2 shows the prior PDFs for Pb isotopes with $98 \leq N \leq 102$, obtained by the QIBP and CBP method. In Fig. 2(a), the CBP estimator employs Gaussian KDE to derive the prior PDFs of the mass residuals. These PDFs exhibit a single, smooth peak that primarily reflects the overall spatial distribution of the data. The construction of such PDFs is heavily influenced by adjacent nuclei. It therefore severely underestimates the impact of nuclei that are strongly correlated but not directly adjacent, such as the nuclei with the same parity of Z and N .

By contrast, the prior PDFs calculated by Eq. (14) of the QIBP algorithm in Fig. 2(b) exhibit a more complex structure. This is because these PDFs incorporate quantum dynamical principles and contain the second derivatives of ψ , which provide enhanced sensitivity to curvature and reveal patterns that KDE cannot capture. This sensitivity is crucial for identifying structures such as shell effects and odd-even staggering. Nuclear mass residuals for nuclei with the same parity of Z and N , mirror nuclei, or other strongly correlated nuclei tend to form clusters. The potential function identifies these clusters, yields lower potential energy, and forms potential wells. Since lower energy corresponds to higher probability density in the Boltzmann distribution, the result-

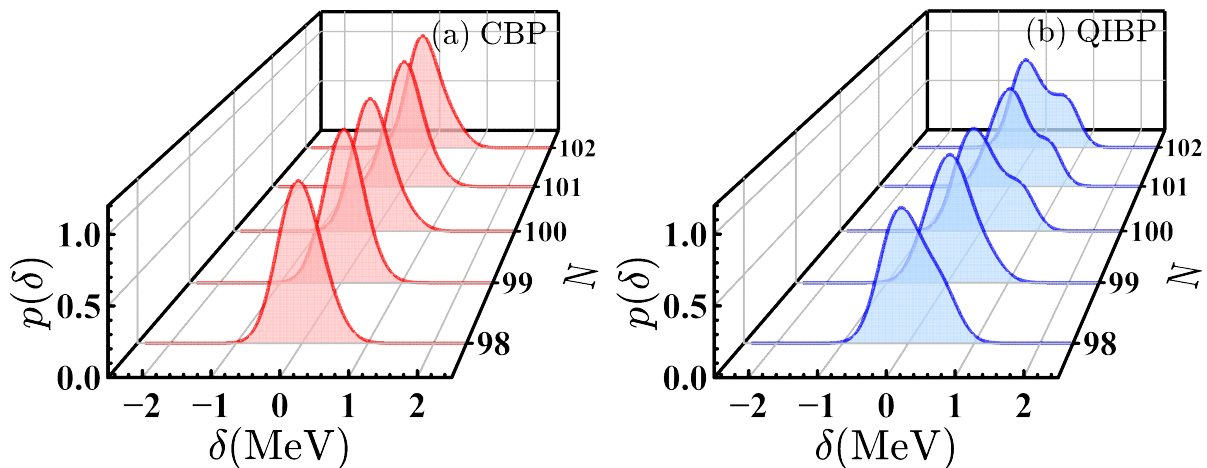


FIG. 2. (a) Prior PDFs for Pb isotopes with $98 \leq N \leq 102$, obtained by the CBP estimator. (b) Prior PDFs for the same nuclei, calculated using the QIBP algorithm.

ing PDFs exhibit local maxima at the positions of these potential wells. These PDFs strengthen the influence of strongly correlated nuclei on the prediction rather than merely fitting the spatial distribution of data. Therefore, the PDFs employed by the QIBP algorithm are more suitable for nuclear mass prediction tasks than those of the CBP estimator.

Extending the above discussion, The one-neutron separation energies S_n for Pb isotopes are derived from the nuclear masses obtained by the QIBP algorithm, As shown in Fig. 3. Fig. 3 also includes S_n from the WS4 model and the CBP estimator, together with experimental values for comparison. In Fig. 3, the WS4 model systematically underestimates S_n for even- N nuclei and overestimates S_n for odd- N nuclei, indicating that part of its deviation arises from odd-even staggering. After optimization by the QIBP algorithm, the description of S_n for each nucleus is improved and performs significantly better than the CBP estimator. These results indicate that the PDFs incorporating quantum dynamical principles account for complex and subtle correlations in nuclear mass data, thereby reliably capturing quantum effects such as odd-even staggering. In contrast, the predictions of the CBP estimator are overly influenced by adjacent nuclei, which weakens its ability to observe odd-even effects. As a result, The QIBP algorithm enable more robust descriptions of nuclear masses and separation energies.

B. Extrapolating capabilities of the QIBP algorithm

Evaluating the performance of the QIBP algorithm when facing unknown data is important. In this section, the extrapolation capability of the QIBP algorithm is analyzed. The learning set consists of 2183 nuclear masses from AME2016 with $Z \geq 20$ and $N \geq 20$ [90].

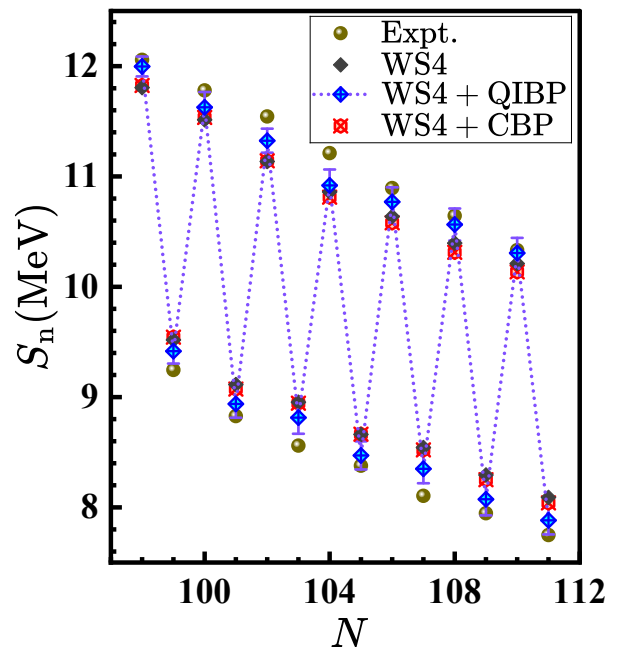


FIG. 3. One-neutron separation energies S_n (MeV) for Pb isotopes. Brown circles denote experimental data, blue diamonds with error bars represent the S_n values and corresponding uncertainties obtained using the QIBP algorithm, and red circles and brown diamonds correspond to the results from the CBP estimator and the WS4 model, respectively.

The validation set is composed of 70 newly added nuclei in AME2020. Table II presents the standard deviations σ^{pre} and σ^{post} for both the learning and validation sets, before and after applying the QIBP algorithm, along with the improvement rates $\Delta\sigma/\sigma^{\text{pre}}$.

According to Table II, for the WS4 model, although the standard deviation on the validation set is slightly lower than that on the learning set, it remains at a relatively

TABLE II. Raw standard deviations σ_{pre} (MeV) from the WS4 and HFB models and the standard deviations σ_{post} (MeV) after QIBP algorithm refinements. The learning set includes 2183 nuclei with $Z \geq 20$ and $N \geq 20$ from AME2016, and the validation set includes the newly added 70 nuclei in AME2020.

Methods	Models	Learning set			Validation set		
		σ_{pre}	σ_{post}	$\Delta\sigma/\sigma_{\text{pre}}$	σ_{pre}	σ_{post}	$\Delta\sigma/\sigma_{\text{pre}}$
QIBP	WS4	0.270	0.150	44.4%	0.355	0.216	39.2%
	HFB	5.210	0.335	93.6%	6.367	0.676	89.4%
CBP	WS4	0.270	0.193	28.5%	0.355	0.255	28.2%
	HFB	5.210	0.526	89.9%	6.367	0.971	84.7%

high precision level of 0.355 MeV. This suggests that the theoretical model possesses a certain extrapolation capability. After refinement by the QIBP algorithm, the posterior standard deviation σ^{post} in the validation set is reduced to 0.216 MeV, corresponding to an improvement rate of 39.2%. Compared with the learning set, the improvement rate decreases by only 5.2%, demonstrating that the QIBP algorithm retains extrapolation ability when applied to the WS4 model. For the HFB model, its original results yield nearly identical values of σ^{pre} for the learning and validation sets, indicating a reasonable degree of extrapolation. After optimization by the QIBP algorithm, the standard deviation in the validation set is reduced to 0.676 MeV, achieving an improvement rate of 89.4%. Although σ^{post} increases compared with the learning set, the improvement remains about 90% and markedly enhancing the HFB model’s description of nuclear masses. Table II also presents the extrapolation performance of the CBP estimator, indicating that the QIBP algorithm provides more reliable predictions for unknown nuclei than the CBP estimator.

The results demonstrate that, on the basis of the global description provided by theoretical models, the QIBP algorithm can further improve nuclear mass predictions for nuclei located at the boundary of the known region. This is because the QIBP algorithm constructs PDFs using more effective Schrödinger potentials, enabling accurate modeling of nuclear mass residual distributions. In addition, Bayesian theory can also analyze the statistical correlations of nuclear masses. Consequently, the QIBP algorithm, embedded with quantum dynamical principles, is capable of detecting effects not incorporated into theoretical models, such as deformation, odd-even staggering, and shell effect. However, the QIBP algorithm also has certain limitations in regions where nuclear mass data are scarce. The absence of nuclides with the same proton or neutron number as the target nucleus in the dataset will result in a reduction in the applicability of the QIBP algorithm. As more experimental mass data become available, the extrapolation capability of the QIBP algorithm is expected to be further enhanced.

C. Further extrapolation of the QIBP algorithm across the nuclear chart

This section examines the extrapolation performance of the QIBP algorithm across the entire nuclear chart, from the boundary of the known region to the drip line. Since the experimental nuclear mass data compiled in AME2020 are relatively limited, the nuclear masses predicted by the WS4 model are used as a “synthetic experimental set”. The HFB model serves as the theoretical model to be optimized. The learning set includes 2253 nuclei from AME2020 with $Z \geq 20$ and $N \geq 20$, while the validation set comprises 2297 nuclei within the drip line determined by the HFB model, covering $20 \leq Z \leq 110$ and $20 \leq N \leq 160$.

Given that the WS4 and HFB models are based on different physical assumptions, the standard deviation between their predictions of the nuclear mass in the validation set is $\sigma_{\text{pre}} = 10.660$ MeV. After applying the QIBP algorithm, the standard deviation is reduced to $\sigma_{\text{post}} = 4.532$ MeV, which represents a 57.5% decrease compared with σ_{pre} . Fig. 4(a) further analyzes the improvement ratio $\Delta\delta/\delta^{\text{pre}} = (|\delta^{\text{pre}}| - |\delta^{\text{post}}|)/|\delta^{\text{pre}}|$ of the QIBP algorithm for each nucleus, where δ^{post} represents the nuclear mass residual after optimization by the QIBP algorithm. In Fig. 4(a), the QIBP algorithm achieves broad improvement across the nuclear chart. The black crosses marks nuclei with $\Delta\delta/\delta^{\text{pre}} \geq 80\%$, which are uniformly distributed around the known region, indicating that the QIBP algorithm significantly improves the theoretical models’ predictions of nuclear masses in these regions.

From the above discussion, it is clear that the QIBP algorithm can provide reliable nuclear mass predictions for nuclei near the experimentally known region. For nuclei far from the known region, although the QIBP algorithm globally adjusts HFB predictions toward the WS4 results, its ability to capture subtle physical effects in distant regions remains limited. This is because no nearby nuclei in the learning set can provide physical information about residual variations in these regions, which prevents the QIBP algorithm from capturing finer physical effects.

Additionally, the same validation is performed for the CBP estimator. The σ^{post} obtained by the CBP estimator is 5.441 MeV, representing a 49.0% decrease compared with σ^{pre} . This indicates that the overall performance of the CBP estimator is weaker than that of the QIBP algorithm. Fig. 4(b) shows the optimization results of the CBP estimator in different regions. It can be seen that the QIBP algorithm exhibits more broadly and uniformly distributed regions with $\Delta\delta/\delta^{\text{pre}} \geq 80\%$ than the CBP estimator, especially in the regions with $N \leq 90$. Moreover, at the edges of the known region, the QIBP algorithm exhibits fewer areas with $\Delta\delta/\delta^{\text{pre}} \leq 0\%$ compared with the CBP estimator. This is due to the QIBP algorithm employing a more robust potential function to process nuclear mass data. It effectively accounts

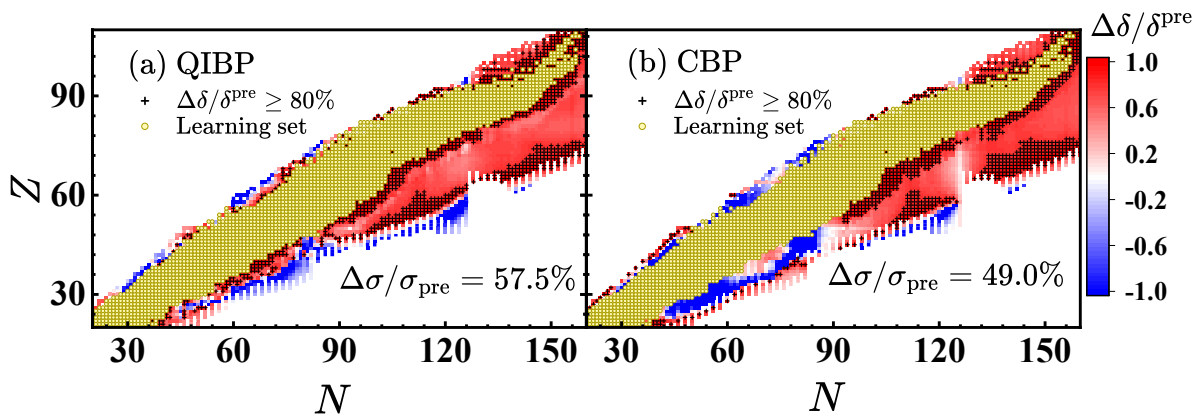


FIG. 4. (a) Improvement ratio $\Delta\delta/\delta^{\text{pre}}$ for each nucleus in the validation set obtained by the QIBP algorithm, with the values mapped to colors according to the color bar on the right. The black crosses denote nuclei with $\Delta\delta/\delta^{\text{pre}} \geq 80\%$. The “synthetic experimental set” corresponds to nuclear masses predicted by the WS4 model, while the theoretical model to be optimized is the HFB model. The learning set includes 2253 nuclei from AME2020 with $Z \geq 20$ and $N \geq 20$, which are marked by khaki circles. The validation set comprises 2297 nuclei within the drip line determined by the HFB model, covering $20 \leq Z \leq 110$ and $20 \leq N \leq 160$. (b) Same as (a), but for the CBP estimator.

for more complex correlations and patterns in nuclear mass data and thus achieves better extrapolation than the CBP estimator.

D. Predictions of α -decay energy based on the QIBP algorithm

This section analyzes the predictive capability of the QIBP algorithm for α -decay energy Q_α . As a key quantity derived from nuclear mass, Q_α serves as an essential input for studying the α -decay process [91, 92]. Due to the logarithmic dependency of the α decay half-life $T_{1/2}$ on Q_α , as described by the Geiger-Nuttall law, even minor deviations in the predicted Q_α can result in significant differences in the calculated $T_{1/2}$ [93]. Furthermore, accurate Q_α values are indispensable for probing the properties of superheavy nuclei [94], understanding the shell structure [95], and identifying new nuclides [96]. Q_α values for the Ra and Es isotopic chains are calculated using the QIBP algorithm based on the WS4 model, as shown in Fig. 5. In this study, Q_α values are derived from the nuclear masses obtained with the QIBP algorithm, thereby demonstrating the capability of QIBP to improve the WS4 model’s description of nuclear mass variations. The corresponding uncertainty is determined using Eq. (20) of the one-sigma uncertainty of the nuclear mass with the standard error-propagation formula. For comparison, Fig. 5 also includes the results of Q_α from CBP estimator and the original results from the WS4 model.

Fig. 5 shows that the WS4 model successfully captures the overall trend of Q_α variations, but discrepancies persist in specific regions. For Ra isotopes, the WS4 model accurately reproduces the sharp increase in Q_α at $N = 126$ associated with shell closure. However, in

the neutron-deficient region, its original predictions deviate to some extent from the experimental values. For Es isotopes, many studies have verified the presence of a subshell at $N = 152$ [97–99], which is manifested as an enhancement in Q_α . Fig. 5(b) indicates that the original predictions of the WS4 model do not fully account for the subshell effect in this region.

After optimization by the QIBP algorithm, the description of Q_α is improved for nearly all nuclei. For Ra isotopes, the QIBP algorithm applies slight adjustments to the WS4 predictions, making them more consistent with the experimental values. For Es isotopes, the improvement achieved by the QIBP algorithm is likewise evident, yielding a more accurate description of the subshell effect at $N = 152$. This improvement is attributed to the incorporation of quantum dynamical principles into the learning process. By processing nuclear data through robust Schrödinger potentials, the QIBP algorithm effectively identifies correlations and patterns among nuclei, thereby capturing quantum features such as subshell effects and yielding more reliable predictions.

To further demonstrate the advantage of the QIBP algorithm in identifying quantum effects, Fig. 5 also presents the Q_α predictions obtained using the CBP estimator. It can be seen that, for both Ra and Es isotopes, the Q_α values predicted by the QIBP algorithm are more consistent with the experimental values than those predicted by the CBP estimator. In particular, for the Es isotopes at $N = 152$, the QIBP algorithm captures the influence of the subshell effect on Q_α more accurately than the CBP estimator. This is because the QIBP algorithm employs a potential function that incorporates quantum dynamical principles to process nuclear data, effectively accounting for the influences of strongly correlated nuclei. As a result, it provides a more reliable description of quantum effects, such as subshell struc-

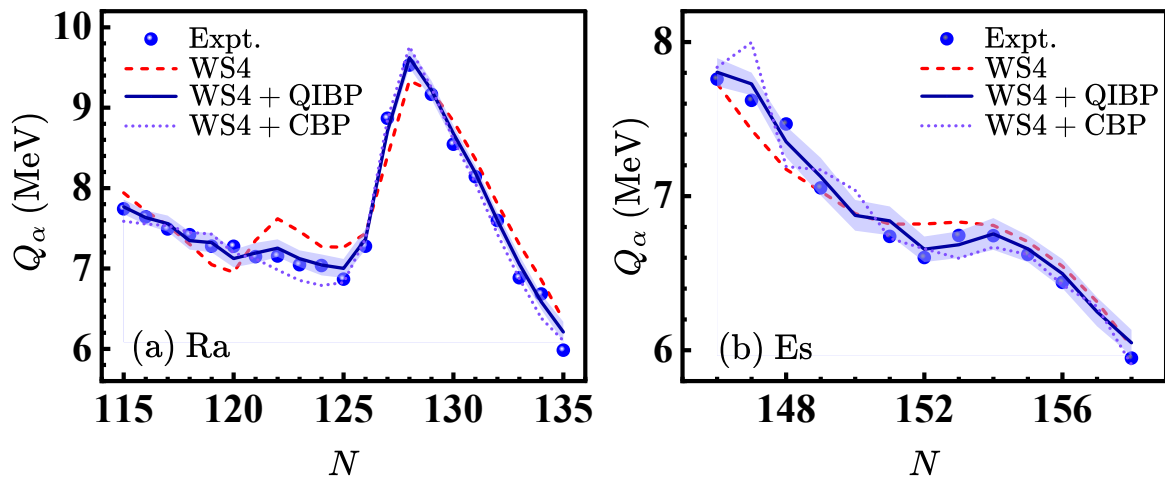


FIG. 5. (a) α -decay energies Q_α (MeV) for the Ra isotope chain. The blue sphere represent experimental values, the red curve shows the original predictions from the WS4 model, the blue curve shows the results after optimization by the QIBP algorithm. The blue dotted line denotes the Q_α values obtained by optimizing WS4 with the CBP estimator. (b) The same as (a), but for the Es isotope chain.

tures. In contrast, the predictions of the CBP estimator rely excessively on adjacent nuclei, which reduces the influence of strongly correlated but non-adjacent nuclei on the prediction and thus weakens its ability to capture quantum effects.

IV. CONCLUSION

In this study, a novel quantum-inspired Bayesian probability (QIBP) algorithm is proposed to optimize theoretical nuclear mass models. In global optimization, the QIBP algorithm achieves improvements of 45.4% for the WS4 model and 93.8% for the HFB model, reducing their standard deviations to 0.149 MeV and 0.324 MeV, respectively. In extrapolation analysis, the improvements remain substantial at 39.2% for WS4 model and 89.4% for HFB model, confirming the extrapolation capability of the QIBP algorithm. Additionally, extrapolation using a synthetic experimental set demonstrates that the QIBP algorithm can significantly improve the description of nuclear masses near the boundary of the known region. Furthermore, the QIBP algorithm improves the WS4 model's predictions of α -decay energies and provides a more reliable description of shell effects.

The effectiveness of the QIBP algorithm can be at-

tributed to its theoretical framework. Specifically, the algorithm maps nuclear mass residuals into Hilbert space and derives probability density functions through wave functions, Schrödinger potentials, and the Boltzmann distribution. By embedding quantum dynamical principles into the learning process, the QIBP algorithm can effectively capture variations in nuclear masses arising from quantum effects such as shell structure, odd-even staggering, and deformation. In summary, the QIBP algorithm is successfully applied to nuclear mass predictions and can provide reliable results for unknown nuclei near the experimentally known region. This algorithm also exhibits scalability and can be applied to future research in other fields such as nuclear reactions and astrophysics.

ACKNOWLEDGEMENTS

This work was supported by the National Natural Science Foundation of China (Grants No. 12475135, No. 12035011 and No. 12475119), by the Shandong Provincial Natural Science Foundation, China (Grant No. ZR2020MA096), and by the Fundamental Research Funds for the Central Universities (Grant No. 22CX03017A).

- [1] M. I. Jordan and T. M. Mitchell, *Science* **349**, 255 (2015).
- [2] G. Carleo, I. Cirac, K. Cranmer, L. Daudet, M. Schuld, N. Tishby, L. Vogt-Maranto, and L. Zdeborová, *Rev. Mod. Phys.* **91**, 045002 (2019).
- [3] K. T. Butler, D. W. Davies, H. Cartwright, O. Isayev, and A. Walsh, *Nature* **559**, 547 (2018).

- [4] J. G. Greener, S. M. Kandathil, L. Moffat, and D. T. Jones, *Nat. Rev. Mol. Cell Biol.* **23**, 40 (2022).
- [5] <https://www.nobelprize.org/prizes/physics/2024>.
- [6] J. J. Hopfield, *Proc. Natl. Acad. Sci.* **79**, 2554 (1982).
- [7] D. E. Rumelhart, G. E. Hinton, and R. J. Williams, *Nature* **323**, 533 (1986).

- [8] G. Hinton, *Rev. Mod. Phys.* **97**, 030502 (2025).
- [9] J. J. Hopfield, *Rev. Mod. Phys.* **97**, 030501 (2025).
- [10] <https://www.nobelprize.org/prizes/chemistry/2024>.
- [11] A. W. Senior, R. Evans, J. Jumper, J. Kirkpatrick, L. Sifre, T. Green, C. Qin, A. Židek, A. W. R. Nelson, A. Bridgland, *et al.*, *Nature* **577**, 706 (2020).
- [12] M. Baek, F. DiMaio, I. Anishchenko, J. Dauparas, S. Ovchinnikov, G. R. Lee, J. Wang, Q. Cong, L. N. Kinch, R. D. Schaeffer, *et al.*, *Science* **373**, 871 (2021).
- [13] J. Jumper, R. Evans, A. Pritzel, T. Green, M. Figurnov, O. Ronneberger, K. Tunyasuvunakool, R. Bates, A. Židek, A. Potapenko, *et al.*, *Nature* **596**, 583 (2021).
- [14] C. H. Bennett and D. P. DiVincenzo, *Nature* **404**, 247 (2000).
- [15] D. Deutsch, *Proc. R. Soc. Lond. A* **400**, 97 (1985).
- [16] L. K. Grover, *Phys. Rev. Lett.* **79**, 325 (1997).
- [17] V. Havlíček, A. D. Córcoles, K. Temme, A. W. Harrow, A. Kandala, J. M. Chow, and J. M. Gambetta, *Nature* **567**, 209 (2019).
- [18] A. Das and B. K. Chakrabarti, *Rev. Mod. Phys.* **80**, 1061 (2008).
- [19] J. Biamonte, P. Wittek, N. Pancotti, P. Rebentrost, N. Wiebe, and S. Lloyd, *Nature* **549**, 195 (2017).
- [20] M. Cerezo, G. Verdon, H.-Y. Huang, L. Cincio, and P. J. Coles, *Nat. Comput. Sci.* **2**, 567 (2022).
- [21] M. Sajjan, J. Li, R. Selvarajan, S. H. Sureshbabu, S. S. Kale, R. Gupta, V. Singh, and S. Kais, *Chem. Soc. Rev.* **51**, 6475 (2022).
- [22] K. T. Schütt, M. Gastegger, A. Tkatchenko, K.-R. Müller, and R. J. Maurer, *Nat. Commun.* **10**, 5024 (2019).
- [23] W. Guan, G. Perdue, A. Pesah, M. Schuld, K. Terashi, S. Vallecorsa, and J. R. Vlimant, *Mach. learn. sci. technol.* **2**, 011003 (2021).
- [24] A. Blance and M. Spannowsky, *J. High Energy Phys.* **2021** (2), 212.
- [25] S. Y. C. Chen, T. C. Wei, C. Zhang, H. Yu, and S. Yoo, *Phys. Rev. Res.* **4**, 013231 (2022).
- [26] P. Duckett, G. Facini, M. Jastrzebski, S. Malik, T. Scanlon, and S. Rettie, *Phys. Rev. D* **109**, 052002 (2024).
- [27] Y. A. Chen and K. F. Chen, *Phys. Rev. D* **111**, 016020 (2025).
- [28] J. D. Martín-Guerrero and L. Lamata, *Neurocomputing* **470**, 457 (2022).
- [29] S. Lloyd, M. Mohseni, and P. Rebentrost, *Nat. Phys.* **10**, 631 (2014).
- [30] Z. K. Li, Z. H. Chai, Y. H. Guo, W. T. Ji, M. Q. Wang, F. Z. Shi, Y. Wang, S. Lloyd, and J. F. Du, *Sci. Adv.* **7**, eabg2589 (2021).
- [31] E. Tang, *Phys. Rev. Lett.* **127**, 060503 (2021).
- [32] M. H. Gordon, M. Cerezo, L. Cincio, and P. J. Coles, *PRX Quantum* **3**, 030334 (2022).
- [33] P. Rebentrost, M. Mohseni, and S. Lloyd, *Phys. Rev. Lett.* **113**, 130503 (2014).
- [34] Z. K. Li, X. M. Liu, N. Y. Xu, and J. F. Du, *Phys. Rev. Lett.* **114**, 140504 (2015).
- [35] G. Gentinetta, A. Thomsen, D. Sutter, and S. Woerner, *Quantum* **8**, 1225 (2024).
- [36] D. Horn and A. Gottlieb, *Phys. Rev. Lett.* **88**, 018702 (2001).
- [37] M. Weinstein and D. Horn, *Phys. Rev. E* **80**, 066117 (2009).
- [38] Z. Y. Han, J. Wang, H. Fan, L. Wang, and P. Zhang, *Phys. Rev. X* **8**, 031012 (2018).
- [39] R. Orús, *Nat. Rev. Phys.* **1**, 538 (2019).
- [40] D. Lunney, J. M. Pearson, and C. Thibault, *Rev. Mod. Phys.* **75**, 1021 (2003).
- [41] J. Erler, N. Birge, M. Kortelainen, W. Nazarewicz, E. Olsen, A. M. Perhac, and M. Stoitsov, *Nature* **486**, 509 (2012).
- [42] Y. Yu, Y. M. Xing, Y. H. Zhang, M. Wang, X. H. Zhou, J. G. Li, H. H. Li, Q. Yuan, Y. F. Niu, Y. N. Huang, *et al.*, *Phys. Rev. Lett.* **133**, 222501 (2024).
- [43] T. Otsuka, A. Gade, O. Sorlin, T. Suzuki, and Y. Utsuno, *Rev. Mod. Phys.* **92**, 015002 (2020).
- [44] A. Gelberg, H. Sakurai, M. W. Kirson, and S. Heinze, *Phys. Rev. C* **80**, 024307 (2009).
- [45] J. J. Cowan, C. Sneden, J. E. Lawler, A. Aprahamian, M. Wiescher, K. Langanke, G. Martínez-Pinedo, and F. K. Thielemann, *Rev. Mod. Phys.* **93**, 015002 (2021).
- [46] M. Williams, C. Angus, A. M. Laird, B. Davids, C. A. Diget, A. Fernandez, E. J. Williams, A. N. Andreyev, H. Asch, A. A. Avaa, *et al.*, *Phys. Rev. Lett.* **134**, 112701 (2025).
- [47] P. Klüpfel, P.-G. Reinhard, T. J. Bürvenich, and J. A. Maruhn, *Phys. Rev. C* **79**, 034310 (2009).
- [48] M. Kortelainen, T. Lesinski, J. Moré, W. Nazarewicz, J. Sarich, N. Schunck, M. V. Stoitsov, and S. Wild, *Phys. Rev. C* **82**, 024313 (2010).
- [49] S. E. Agbemava, A. V. Afanasjev, D. Ray, and P. Ring, *Phys. Rev. C* **89**, 054320 (2014).
- [50] A. V. Afanasjev and S. E. Agbemava, *Phys. Rev. C* **93**, 054310 (2016).
- [51] T. Wolfgruber, M. Knöll, and R. Roth, *Phys. Rev. C* **110**, 014327 (2024).
- [52] P. Guo, X. J. Cao, K. M. Chen, Z. H. Chen, M. K. Cheoun, Y. B. Choi, P. C. Lam, W. Deng, J. Dong, P. Du, *et al.*, *At. Data Nucl. Data Tables* **158**, 101661 (2024).
- [53] P. Becker, D. Davesne, J. Meyer, J. Navarro, and A. Pastore, *Phys. Rev. C* **96**, 044330 (2017).
- [54] J. Geng, Z. H. Wang, P. W. Zhao, Y. F. Niu, H. Liang, and W. H. Long, *Phys. Rev. C* **111**, 024305 (2025).
- [55] G. T. Garvey, W. J. Gerace, R. L. Jaffe, I. Talmi, and I. Kelson, *Rev. Mod. Phys.* **41**, S1 (1969).
- [56] M. Bao, Z. He, Y. Lu, Y. M. Zhao, and A. Arima, *Phys. Rev. C* **88**, 064325 (2013).
- [57] C. Ma, Y. Y. Zong, Y. M. Zhao, and A. Arima, *Phys. Rev. C* **102**, 024330 (2020).
- [58] S. E. Agbemava, A. V. Afanasjev, D. Ray, and P. Ring, *Phys. Rev. C* **89**, 054320 (2014).
- [59] A. Boehnlein, M. Diefenthaler, N. Sato, M. Schram, V. Ziegler, C. Fanelli, M. Hjorth Jensen, T. Horn, M. P. Kuchera, D. Lee, *et al.*, *Rev. Mod. Phys.* **94**, 031003 (2022).
- [60] W. B. He, Q. F. Li, Y. G. Ma, Z. M. Niu, J. C. Pei, and Y. X. Zhang, *Sci. China Phys. Mech. Astron.* **66**, 282001 (2023).
- [61] K. Gernoth, J. Clark, J. Prater, and H. Bohr, *Phys. Lett. B* **300**, 1 (1993).
- [62] R. Utama, J. Piekarewicz, and H. B. Prosper, *Phys. Rev. C* **93**, 014311 (2016).
- [63] R. Utama and J. Piekarewicz, *Phys. Rev. C* **96**, 044308 (2017).
- [64] Z. M. Niu, J. Y. Fang, and Y. F. Niu, *Phys. Rev. C* **100**, 054311 (2019).
- [65] A. E. Lovell, A. T. Mohan, T. M. Sprouse, and M. R. Mumpower, *Phys. Rev. C* **106**, 014305 (2022).

- [66] A. Sharma, A. Gandhi, and A. Kumar, *Phys. Rev. C* **105**, L031306 (2022).
- [67] Z. S. Jin, M. S. Yan, H. Zhou, A. Cheng, Z. Z. Ren, and J. Liu, *Phys. Rev. C* **108**, 014326 (2023).
- [68] Y. H. Lu, T. S. Shang, P. X. Du, J. Li, H. Z. Liang, and Z. M. Niu, *Phys. Rev. C* **111**, 014325 (2025).
- [69] J. Liu, Z. S. Jin, and Z. Z. Ren, *Phys. Rev. C* **112**, 024309 (2025).
- [70] Z. P. Gao, Y. J. Wang, H. L. Lü, Q. F. Li, C. W. Shen, and L. Liu, *Nucl. Sci. Tech.* **32**, 109 (2021).
- [71] G. P. Liu, H. L. Wang, Z. Z. Zhang, and M. L. Liu, *Phys. Rev. C* **111**, 024306 (2025).
- [72] L. Neufcourt, Y. Cao, W. Nazarewicz, E. Olsen, and F. Viens, *Phys. Rev. Lett.* **122**, 062502 (2019).
- [73] L. Neufcourt, Y. Cao, S. A. Giuliani, W. Nazarewicz, E. Olsen, and O. B. Tarasov, *Phys. Rev. C* **101**, 044307 (2020).
- [74] L. Neufcourt, Y. Cao, S. Giuliani, W. Nazarewicz, E. Olsen, and O. B. Tarasov, *Phys. Rev. C* **101**, 014319 (2020).
- [75] Y. F. Ma, C. Su, J. Liu, Z. Z. Ren, C. Xu, and Y. H. Gao, *Phys. Rev. C* **101**, 014304 (2020).
- [76] Y. F. Liu, C. Su, J. Liu, P. Danielewicz, C. Xu, and Z. Z. Ren, *Phys. Rev. C* **104**, 014315 (2021).
- [77] J. Z. Xie, K. P. Wang, C. Wang, W. Q. Gao, M. Ju, and J. Liu, *Phys. Rev. C* **109**, 064317 (2024).
- [78] J. Liu, K. Z. Tan, L. Wang, W. Q. Gao, T. S. Shang, J. Li, and C. Xu, *Nucl. Sci. Tech.* **36**, 215 (2025).
- [79] X. H. Wu and P. W. Zhao, *Phys. Rev. C* **101**, 051301 (2020).
- [80] Y. Y. Guo, T. Yu, X. H. Wu, C. Pan, and K. Y. Zhang, *Phys. Rev. C* **110**, 064310 (2024).
- [81] Y. M. Huang, J. H. Chen, J. Y. Jia, L. M. Liu, Y. G. Ma, and C. J. Zhang, *Phys. Rev. C* **111**, 034329 (2025).
- [82] Z. M. Niu and H. Z. Liang, *Phys. Rev. C* **106**, L021303 (2022).
- [83] M. Bender, P. H. Heenen, and P. G. Reinhard, *Rev. Mod. Phys.* **75**, 121 (2003).
- [84] K. Blaum, *Phys. Rep.* **425**, 1 (2006).
- [85] N. Wang, M. Liu, X. Z. Wu, and J. Meng, *Phys. Lett. B* **734**, 215 (2014).
- [86] E. Chabanat, P. Bonche, P. Haensel, J. Meyer, and R. Schaeffer, *Nuclear Physics A* **635**, 231 (1998).
- [87] D. H. Ackley, G. E. Hinton, and T. J. Sejnowski, *Cognitive Science* **9**, 147 (1985).
- [88] C. Geng, J. Wang, L. Chen, Z. Y. Gao, J. Frelsen, and S. Hauberg, *Int. J. Comput. Vis.* **133**, 5898 (2025).
- [89] M. Wang, W. Huang, F. Kondev, G. Audi, and S. Naimi, *Chin. Phys. C* **45**, 030003 (2021).
- [90] W. J. Huang, G. Audi, M. Wang, F. G. Kondev, S. Naimi, and X. Xu, *Chin. Phys. C* **41**, 030002 (2017).
- [91] D. D. Ni and Z. Z. Ren, *Nucl. Phys. A* **893**, 13 (2012).
- [92] M. Bao, Z. He, Y. M. Zhao, and A. Arima, *Phys. Rev. C* **90**, 024314 (2014).
- [93] C. Qi, A. Andreyev, M. Huyse, R. Liotta, P. Van Duppen, and R. Wyss, *Phys. Lett. B* **734**, 203 (2014).
- [94] E. Olsen and W. Nazarewicz, *Phys. Rev. C* **99**, 014317 (2019).
- [95] S. L. Tang, Y. B. Qian, T. Wan, and Z. Z. Ren, *Phys. Rev. C* **112**, 014308 (2025).
- [96] J. Hilton, J. Uusitalo, J. Sarén, R. D. Page, D. T. Joss, M. A. M. AlAqeel, H. Badran, A. D. Briscoe, T. Calverley, D. M. Cox, *et al.*, *Phys. Rev. C* **100**, 014305 (2019).
- [97] A. Ghiorso, S. G. Thompson, G. H. Higgins, B. G. Harvey, and G. T. Seaborg, *Phys. Rev.* **95**, 293 (1954).
- [98] H. Makii, T. Ishii, M. Asai, K. Tsukada, A. Toyoshima, M. Matsuda, A. Makishima, J. Kaneko, H. Toume, S. Ichikawa, *et al.*, *Phys. Rev. C* **76**, 061301 (2007).
- [99] B. Y. Chen, J. M. Dong, Y. Q. Wang, and G. Q. Wu, *Chin. Phys. C* **49**, 011001 (2025).